

See discussions, stats, and author profiles for this publication at: <https://www.researchgate.net/publication/256663689>

Photoinduced Charge Transfer in Solvated Anthraquinones Is Facilitated by Low-Frequency Ring Deformations

ARTICLE in THE JOURNAL OF PHYSICAL CHEMISTRY B · SEPTEMBER 2013

Impact Factor: 3.3 · DOI: 10.1021/jp408954p · Source: PubMed

CITATIONS

5

READS

47

4 AUTHORS, INCLUDING:



Ajay Jha

Tata Institute of Fundamental Research

8 PUBLICATIONS 9 CITATIONS

SEE PROFILE



Debayan Chakraborty

University of Cambridge

6 PUBLICATIONS 33 CITATIONS

SEE PROFILE

Photoinduced Charge Transfer in Solvated Anthraquinones Is Facilitated by Low-Frequency Ring Deformations

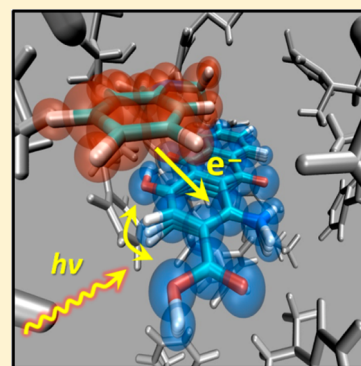
Ajay Jha,^{†,§} Debayan Chakraborty,^{†,§} Varadharajan Srinivasan,^{*,‡} and Jyotishman Dasgupta^{*,†}

[†]Department of Chemical Sciences, Tata Institute of Fundamental Research, Mumbai 400005, India

[‡]Department of Chemistry, Indian Institute of Science Education and Research, Bhopal 462023, India

S Supporting Information

ABSTRACT: Efficiency of photoinduced charge transfer (CT) reactions in supramolecular assemblies is often compromised due to the rigid parametrization of acceptable donor–acceptor (D–A) distances and orientations. Using a combined approach of time-resolved optical measurements and electronic structure studies guided by molecular dynamics (MD) simulations, we demonstrate that dynamic control on CT rate exists for quenching of hydroxy-anthraquinones in donor aniline-like solvents. We find that anthraquinone ring deformation modes control the kinetics of CT within ~ 300 – 700 fs by modulating the D–A electronic couplings. Our work demonstrates that low-frequency motions have to be critically understood for all such D–A pairs, and generates a rational methodology for utilization of hydroxy-anthraquinone acceptors in numerous photoactive architectures.



■ INTRODUCTION

Implementing efficient photoinduced charge separation is the key step toward developing new materials for light energy conversion.^{1–4} Construction of photoactive supramolecular assemblies incorporating through space charge transfer (CT) donor–acceptor (D–A) pairs is usually based on their molecular adaptability (e.g., size and shape) in a scaffold of choice and the relative redox potentials. In such designs, the inefficiencies usually arise from the ambiguity of proper distance and orientation constraints between the D–A pairs, parameters that partly define the charge transfer reaction coordinate.⁵ A critical molecular insight into all the involved reaction coordinates^{6,7} and their dynamic interplay thus becomes imperative to the realization of high quantum yield photomaterials.^{8,9}

Anthraquinones have been used as potent two-electron redox acceptors in various functional complexes^{10,11} and molecular wires¹² due to their intrinsic advantages of small size, planarity, and ease of derivatization. For anthraquinones to be utilized in large structures, the guiding principles can only emerge from a critical evaluation of the non-adiabatic rates, couplings, and transfer pathways in a donor bath with all possible D–A configurations.^{6,7,13–16} Previous studies on fluorescent dyes, e.g., coumarin and oxazine, solvated in electron donor solvents revealed sub-picosecond electron transfer dynamics in such arrangements.^{17–21} A theoretical framework to explain such fast rates argued for a dynamic fluctuation of the CT coupling through solvent and dye vibrational modes.^{22–28}

Motivated by these ideas, we studied visible absorbing amine-functionalized hydroxyanthraquinone acceptors¹¹ solvated in donor solvents with the aim of developing a potential methodology for driving ultrafast CT reactions. Due to the

presence of chemically modifiable amine and hydroxy groups, this class of molecules should inspire synthetic exploration in large functional structures for multielectron reactions. Using a combination of time-resolved electronic and steady state resonance Raman measurements, we show vibration-assisted sub-picosecond CT from the donor to the photoexcited hydroxyanthraquinone ring. Electronic structure calculations guided by classical MD simulations reveal that low-frequency ring deformations are the major players in the attainment of the CT state and the stabilization of the incipient electron on the ring.

■ EXPERIMENTAL SECTION

Chemicals. Anthraquinone derivative (A1) and *N*-methyl-aniline (NMA) were purchased from Sigma Aldrich, USA. Toluene, methanol, aniline, and *N,N*-dimethylaniline (DMA) were purchased from SD Fine-Chem Pvt. Ltd., India.

Steady State Absorption and Emission Measurements. All the absorption measurements were carried out in a JASCO spectrophotometer. The steady state fluorescence measurements of A1 in different solvents were carried out using a SPEX Fluorolog model 1681T (T-format) spectrofluorimeter which uses a high pressure Xe lamp as the excitation source, grating monochromators, and a PMT (Hamamatsu R928A).

Time-Resolved Emission Measurements. Time-resolved fluorescence intensity decay measurements were carried out

Received: September 6, 2013

Revised: September 15, 2013

Published: September 16, 2013



using a commercial femtosecond upconversion setup (FOG 100) which has been described in detail elsewhere.²⁹

For fluorescence upconversion measurements, the output of a femtosecond pulsed oscillator from a mode-locked Ti:sapphire laser (Tsunami, Spectra Physics) pumped by a 5 W Millennia (Spectra Physics) DPSS laser, centered at 820 nm and with a repetition rate of 100 MHz, is used as the gate pulse for the femtosecond fluorescence upconversion experiments. The second harmonic (410 nm) of this pulse has been used as the source of excitation for the sample placed in a rotating cell. The incident power of second harmonic light at the sample was attenuated to 10 mW in order to minimize photobleaching. The fluorescence emitted from the sample is upconverted in a nonlinear crystal by mixing with the gate pulse, which consists of a portion of the fundamental beam. The upconverted light was dispersed onto a monochromator and detected using photon counting electronics. A two-pulse cross-correlation experiment using the Raman scattering from ethanol was carried out to obtain the instrument response function (IRF) of ~ 340 fs. The femtosecond fluorescence decays have been fitted using a Gaussian function of the same fwhm as the excitation pulse. The fluorescence decays have been recorded at the magic angle polarization with respect to the excitation pulse.

Pump–Probe Measurements. All pump–probe measurements were carried out using an amplified laser source. The 400 mW output power from a commercial oscillator (Micra-5 mode-locked titanium:sapphire operating at 80 MHz repetition rate) with a bandwidth of ~ 100 nm was amplified using a regenerative amplifier (Coherent Legend Elite) to produce ~ 30 fs amplified pulses at a repetition rate of 1 kHz. The 4 mJ/pulse amplified light was split into two portions for the generation of the tunable pump and probe pulses. The 490 nm pump pulse was generated using an optical parametric amplifier (Coherent OPeraASolo Ultrafast Optical Parametric Amplifier system) and attenuated to ~ 100 – 200 nJ. The white-light probe continuum (420–750 nm) was generated using a 2 mm thick sapphire crystal. The actinic pump and probe pulses were focused and overlapped within the sample inside a flow cuvette with 0.5 mm glass window. The probe light was detected using a multichannel detector procured from Ultrafast Systems, Sarasota, FL, as part of their Helios spectrometer. The pump–probe pulse delay was controlled with a motorized translation stage outfitted with a quadra-pass mirror assembly. Polarizations of the pulses were kept vertical in most of the measurements. Any effect of rotational diffusion was checked by orienting the pump polarization at the magic angle (54.7°). The wavelength sensitive instrument response function (IRF) was measured using an optical Kerr-effect (OKE) arrangement on a 1 mm glass with a pair of polarizer (in pump path) and analyzer (in the probe path). The measurements were done using a 1 mm flow-cell with a 0.5 mm thick quartz window. The flow rate was adjusted to replenish fresh sample before each laser shot. The temporal instrument response is a Gaussian, with a fwhm of ~ 90 fs as measured by the optical Kerr effect. The $t = 0$ time delay was initially set by the cross-correlation and the comparison to the solvent response but was allowed to vary freely in the fitting of the kinetics. All kinetic data were fitted using a two- or three-exponential decay model convoluted with the IRF using home written codes in IGOR 5 Pro. The singular value decomposition of the transient data was carried out by using the Surface Explorer software from Ultrafast Systems.

Resonance Raman Measurements. Resonance Raman spectra at 514.5, 647.1, and 632.8 nm excitation wavelengths were recorded using an inverted microscope setup (with back scattering geometry) attached to a triple grating spectrometer (Horiba Jobin Yvon T64000) and a liquid-nitrogen-cooled CCD detector. The powers used at the sample for these wavelengths were 1.5, 11.0, and 4.5 mW, respectively. Excitation wavelengths of 514.5 and 647.1 nm were taken from a mixed $\text{Ar}^+ - \text{Kr}^+$ ion mixed gas laser (Spectra Physics, Stabilite 2018). The 632.8 nm excitation wavelength was taken from a He–Ne laser (Coherent Inc.). The laser beam was focused on the sample using a $10\times$ objective.

Raman excitation at 532 nm was generated from a solid-state frequency doubled Nd:YAG laser (model G-SLM-015, Suwtech Inc., China). Details of the setup used have been described elsewhere.³⁰ Briefly, a special Ag-coated mirror was used to reflect the laser beam by 45° to focus onto the sample using a $50\times$ objective. The back scattered light was put into the spectrograph (Jobin-Yvon 550 Triax, Instruments SA, Inc., NJ) using an optical fiber. The spectrograph was attached with a liquid-nitrogen-cooled CCD detector. A holographic 600 grooves/mm grating was used along with the $200\ \mu\text{m}$ spectrograph entrance slit setting, providing $\sim 5\ \text{cm}^{-1}$ resolution. Raman spectra were plotted after solvent subtraction. All the measurements were carried out in a capillary based rapid flow system driven by a peristaltic pump.

Cyclic Voltammetry Measurements. Cyclic voltammograms of A1 in methanol shown in Figure S7 (Supporting Information) were recorded on an Electrochemical Analyzer, CH Instruments, between 0.0 and -1.6 V at a scan rate of 10 mV/s. For measurements, a bare glassy carbon (GC) electrode was used as the working electrode and a platinum wire as the counter electrode. To polish the working electrode, alumina powder was used which was further washed with water and acetone before using it. Ag/AgCl (standard) was used as the reference electrode. Tetrabutyl ammonium perchlorate (TBAP, Fluka) was used as the supporting electrolyte in ~ 0.1 M concentration. The voltammogram shows one cathodic peak and two anodic peaks representing irreversibility of the second peak. The reduction potential of A1 was calculated to be -0.55 V vs Ag/AgCl electrode.

■ COMPUTATIONAL SECTION

Computational Methodology. The ultrafast electron transfer reaction involving the organic A1 solvated in DMA was modeled using a combination of classical molecular dynamics (MD) and time-dependent density functional theory (TDDFT). The general strategy chosen employed the following three steps: (1) generate a classical MD trajectory of A1 solvated in DMA, in particular, to identify the first solvation shell, (2) compute electronic coupling matrix elements of A1–DMA pairs in the first solvation shell using the TDDFT approach, and (3) project the MD trajectory along normal modes of A1, and study the correlation between the mode amplitudes and the electronic coupling elements. Below, we present a description of the methodology followed in each of these steps. The results and the observed correlations are discussed in the next section.

(1). *MD Simulations.* The gas phase optimized structures of the dye and the solvent molecule at the B3LYP/6-311G(d,p) level, obtained using the GAUSSIAN09 package, served as the starting structures of the MD simulations.³¹ The system of A1 solvated in DMA was realized by placing a single solute

molecule at the center of a 50 Å box containing 587 DMA molecules corresponding to a pure solvent density of 0.95 g/cm³.³² All the interactions were parametrized according to the OPLS-AA^{32,33} force field. Before the dynamics simulations, the solvent box containing the solute was minimized using steepest descent and conjugate gradient methods as available within the GROMACS-3.4.1 distribution.^{34,35} This was followed by 500 ps of equilibration in the NPT ensemble employing the velocity rescaling algorithm to maintain the temperature at 298 K and the Berendsen barostat³⁶ to maintain pressure control at 1 bar. A time step of 1 fs was used for integration using the leapfrog scheme. The equilibration run was followed by 500 ps of NVT dynamics employing the Nosé–Hoover thermostat^{37,38} at 298 K. During all the simulations, the hydrogen bonds were constrained using the LINCS algorithm.³⁹

Our MD simulations enabled us to sample a large part of the thermally accessible configuration space of the dye solvated in DMA. The last 9 ps of the trajectory was considered for subsequent analysis. In this window, we considered all DMA molecules which visited the first solvation shell of the solvated dye during the dynamics for computing electronic coupling matrix elements using the generalized Mulliken–Hush (GMH) approach⁴⁰ in a pairwise fashion. As highlighted in the Results and Discussion section, we used this trajectory to look at the distribution of electronic coupling elements as a function of orientation and distance for all the possible solute–solvent pairs with a sampling interval of 1 ps. We selected the solute–solvent pair which showed the highest value of coupling in these snapshots and further carried out short NVE simulations around this geometry on a much finer time scale of 25 fs to explore the possible correlations between these vibrational fluctuations and dynamical nature of the CT coupling. This ensured that, while correlating dynamic electron transfer couplings and amplitudes of vibrational motions, we are effectively sampling geometries which are in the regions of the configuration space favoring ultrafast ET reactions.

(2). *Generalized Mulliken Hush Analysis.* The charge transfer couplings were computed according to the generalized Mulliken–Hush (GMH) formalism proposed by Cave and Newton.⁴⁰ It is computed as follows:

$$H_{\text{DA}} = \frac{m_{\text{DA}} \Delta E_{\text{DA}}}{\sqrt{(\Delta \mu_{\text{DA}})^2 + 4(m_{\text{DA}})^2}}$$

where H_{DA} is the electronic coupling, m_{DA} is the transition dipole moment connecting the two states, $\Delta \mu_{\text{DA}}$ is the dipole moment difference between the two states, and ΔE_{DA} is the energy gap between the initial and final adiabatic states.

The dipole moments and excitations out of the ground state were estimated within the formalism of linear-response time-dependent density functional theory (LR-DFT).⁴¹ The excitations correspond to the poles of the linear response function, and the corresponding residues give the transition moments connecting the excited states to the ground states. In order to compute the transition moments connecting two excited states, one has to go beyond the linear response regime and consider higher order corrections to the Hamiltonian arising due to the time-dependent perturbation. The double residue of the quadratic response (QR) function corresponds to the transition moment between two excited states.⁴² All the TDDFT calculations⁴³ were computed using the DALTON quantum chemistry package.⁴⁴ The orbitals which are involved in the LE and CT transitions for the A1–DMA 1:1 system are

shown in Figure 6. All the molecular orbitals were plotted using VMD⁴⁵ visualization software at an electronic isodensity of 0.02. Typically, the LE is a HOMO–1 to LUMO transition where the electron densities are localized over the A1 molecule. The CT on the other hand is a HOMO–LUMO transition where the HOMO is delocalized over the DMA molecule.

(3). *Extracting Vibrational Amplitudes from MD Trajectory.* The trajectory from the classical simulations was projected onto the subspace of normal mode eigenvectors of the solute A1. The normal mode amplitudes were computed according to the method suggested by Petrone and Pande.⁴⁶ Before the projections, the overall translations and rotations of the solute were removed. A conformational state B_t of the solute sampled during MD can be expressed in terms of the coordinates of the equilibrium structure A as follows:

$$B_t = A_{\text{eq}} + \sum_{i=1}^N C_i \xi_i^{\text{DFT}}$$

Here C_i corresponds to the amplitude or the contribution of a normal mode represented by the appropriate normal mode vector to the overall conformational change. The eigenvectors which are denoted by ξ_i^{DFT} were computed at the B3LYP/6-311G(d,p) level for the optimized A1 structure in the gas phase.

RESULTS AND DISCUSSION

Steady State Spectroscopy. Our choice of visible absorbing anthraquinone derivative was primarily based on its ease of derivatization for creating functional complexes with anthraquinone as acceptors. We used 1-amino-4-hydroxyanthraquinone-2-carboxylic acid (A1) as an acceptor (Figure 1) to illustrate the charge transfer reaction in donor aniline-like

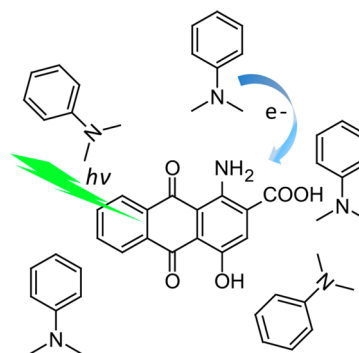


Figure 1. (a) Scheme depicting the photoinduced charge transfer process in a dimethylaniline (DMA) solution of hydroxyanthraquinone A1.

solvents. Due to the –COOH group in the amine containing ring, A1 has a strongly allowed electronic transition in the visible region arising from the delocalized anthraquinone ring electrons. Figure 2a presents absorption spectra of A1 in different solvents. A1 exhibits a strong absorption feature with associated vibrational fine structure in the visible region. The relative insensitivity of this intensely allowed feature in a variety of solvents, e.g., toluene, *N,N*-dimethyl aniline (DMA), and aniline, indicates a localized ring excitation (LE) associated with the delocalized ring electrons of the anthraquinone skeleton. In electron donating solvents like aniline and DMA, the absorption spectrum however appears broader on the red

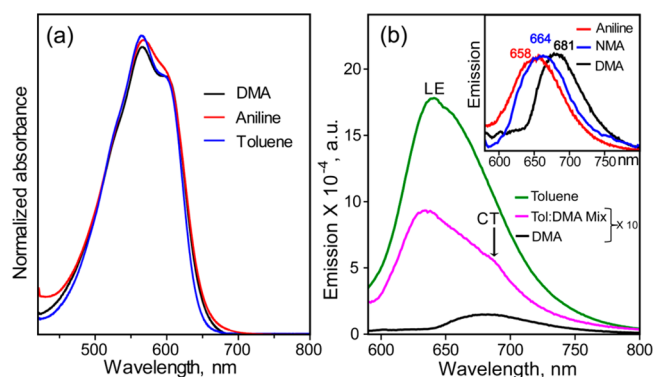


Figure 2. (a) Comparison of the steady-state absorption of A1 in DMA, toluene, and aniline in the visible wavelengths arising from the local excitation. The wings of the absorption profile of A1 in DMA and aniline show a larger intensity as compared to toluene, although the maximum is unaltered. (b) Steady state emission of A1 in toluene, 3:2 toluene/DMA mixture, and 100% DMA. The presence of the shoulder in the mixed toluene/DMA solution indicates CT emission. Inset: Steady state emission of A1 dissolved in pure aniline, *N*-methylaniline (NMA), and *N,N*-dimethylaniline (DMA), respectively.

edge possibly due to an overlapping weakly allowed intermolecular CT transition. In such donor solvents, it is important to characterize the spectroscopic signatures of the CT state, and associate it with specific donor–acceptor complexes.

Steady state emission was used as a probe to monitor the non-radiative pathways on the A1 excited state in electron donating and redox-inert solvents. Figure 2b (main) presents the fluorescence spectra of A1 after excitation at 550 nm in toluene, DMA and a 3:2 v/v mixture of toluene with DMA. The LE emission feature of A1 in toluene appears at 640 nm, and is rather insensitive to solvent polarity of redox-inert solvents (SI, Figure S1). However, the LE feature is partially quenched in the toluene/DMA mixture while complete quenching was observed in pure DMA. Concomitantly, a new feature at 681 nm was observed after quenching which is also present in the mixture indicating emission from an energetically

lower excited state in DMA added samples. The lower emissive state, which is only observed in redox active solvents, was assigned to be the intermolecular CT state,²¹ and confirmed by the solvatochromic shift from 658 to 681 nm in aniline ($\epsilon = 6.7$), *N*-methylaniline ($\epsilon = 6.0$), and DMA ($\epsilon = 4.4$), as shown in the inset of Figure 2b.^{17,47} The intermolecular CT assignment was further bolstered by the expected correlation of the emission maxima with the respective solvent donor oxidation potentials.²⁹ It has been previously reported that the emission maxima of the CT states show a hypsochromic shift upon increasing the donor potentials. Therefore, our steady state data indicates the presence of two emissive states LE and CT whose temporal connectivity evidently reflects the CT reaction.

Time-Resolved Emission Measurements. Kinetics of the implied CT quenching process was determined by recording the time-resolved emission process decays in DMA and aniline using femtosecond fluorescence upconversion with an ~ 340 fs instrument response function (IRF). Figure 3a shows the fluorescence decay profiles recorded at 640 and 630 nm in DMA and aniline, respectively, subsequent to excitation at 410 nm. In DMA, the profile shows a fast $\sim 650 \pm 80$ fs decay along with a slower component of 8.6 ± 1.9 ps which were elucidated by fitting the data to a biexponential model convoluted with the IRF. For A1 in aniline, the two components are found to be 610 ± 15 fs and 7.5 ± 0.4 ps. The goodness of fit for the faster component is illustrated in Figure 3a (inset) which clearly indicates almost similar emission decay rates in both aniline and DMA. However, the shortening of the longer time component indicates polarity dependence, and together with the steady state fluorescence data hints at ground state recovery from the CT state via charge recombination.

Since the steady state emission experiments strongly indicate the presence of two emissive states, the observed time components could be correlated to their individual lifetimes if their amplitude spectra can be matched with their respective emission spectra. Multiwavelength emission kinetics were carried out at five different wavelengths ranging from 630 to 700 nm for A1 solvated in DMA. Global fits to the upconversion decay profiles (Figure S2, Supporting Informa-

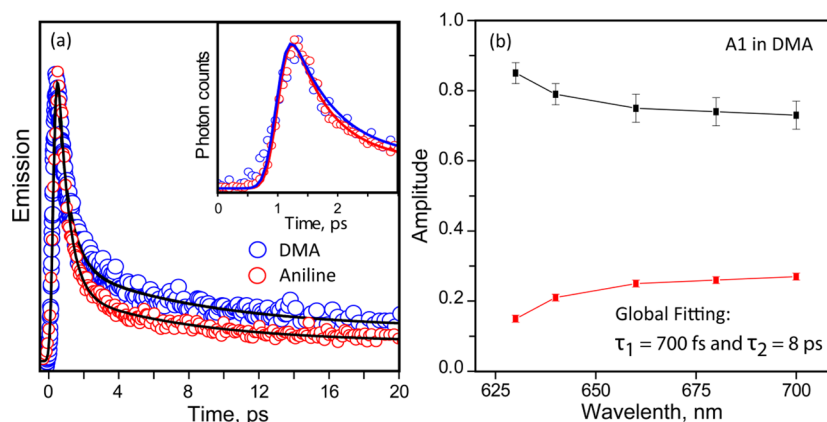


Figure 3. (a) Main: Fluorescence decay profile of A1 in DMA and aniline collected at 640 and 630 nm, respectively, with an excitation at 410 nm. The IRFs of fluorescence upconversion measurements were ~ 370 and ~ 340 fs for 630 and 640 nm, respectively. Data were fitted to a biexponential model with time constants tabulated in the figure. Inset: The early time points are expanded to show the quality of the fits with time constants $\tau_{\text{DMA}} = 650 \pm 80$ fs and 8.6 ± 1.9 ps, while $\tau_{\text{aniline}} = 610 \pm 15$ fs and 7.5 ± 0.4 ps, respectively. (b) Plot of the amplitudes after global fitting of the A1 in DMA data with time constants of 700 fs and 8 ps. The short time constant corresponds to the decay of the LE state which dominates the fluorescence of A1 in the blue region around 630–640 nm. The long time component which corresponds to the weak emission from the CT state absorbs more in the red region, ~ 680 nm.

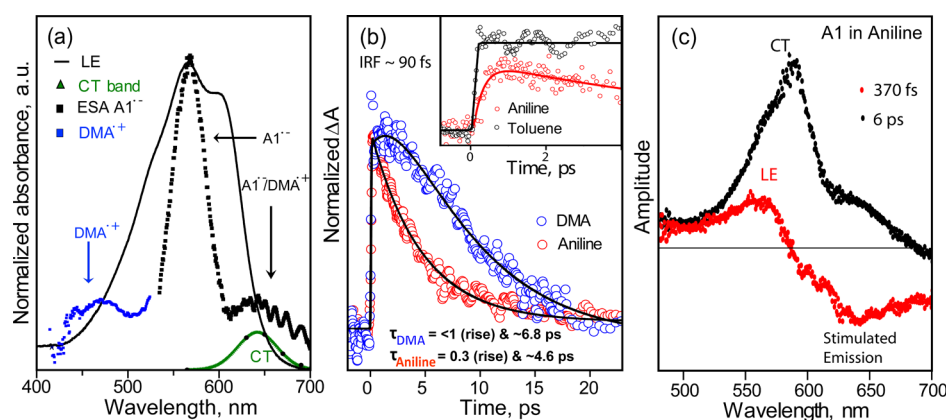


Figure 4. (a) Comparison of the ground state absorption spectrum of A1 (black solid), the intermolecular CT state (black dots, with a Gaussian fit in green), the A1 anion radical absorption (black squares), and the DMA cation radical (blue squares) spectrum. (b) Main: Kinetics of the excited state absorption (ESA) feature of A1 in both aniline (red circles) and DMA (blue circles) obtained at 565 nm from transient pump–probe measurements after 510 nm excitation. A1 shows faster decay kinetics in aniline as compared to in DMA. Inset: Transient spectra of A1 in aniline (red) and DMA (blue) after 1.2 ps. (c) Plot showing the principal components obtained from global fitting of transient spectra obtained for A1 in aniline. Two distinct features are deconvolved with lifetimes of 370 fs and 6 ps which correspond to the LE and CT states, respectively.

tion) were reliably obtained with two exponents of 700 ± 100 fs and 8 ± 2 ps. Figure 3b shows the amplitude spectra of both the short and long components, which correlates well with the spectra of the LE and CT states, respectively. The amplitude of the faster component decreases as the collection wavelength is shifted to the red region. Since the LE is more strongly allowed than the CT, the emission even at 680 nm is dominated by the LE emission which is also reflected in the amplitudes. However, the contribution of the long time component to the emitted photons increases as we shift the photon collection closer to 700 nm. The amplitude spectrum of the 8 ps component provides conclusive evidence for CT emission, and therefore, we unequivocally assigned the ultrafast sub-picosecond component to the electron transfer from the donor solvent to the excited A1 molecule.

Time-Resolved Absorption Spectroscopy. To confirm the assignment of the faster lifetime component to the CT process, identification of the product radical signatures is imperative. Using transient electronic measurements within the probe window 420–700 nm, excited state species subsequent to photoexcitation were detected with an IRF of ~ 90 fs. The evolution of the excited state from LE to CT can be tracked by following the population of the CT state. The CT state should be characterized by the presence of the DMA cation radical and the corresponding A1 anion radical (Figure S3, Supporting Information). Figure 4a shows the transient spectra of the CT state which has spectral features at 470 nm, along with two other features at 568 and 650 nm, respectively. The 470 nm feature in the transient spectrum was assigned to the DMA cation radical, although a weak shoulder (rendered invisible here) in the range 650–800 nm also signifies its presence.^{48,49} The strong feature at 568 nm along with the broad 650 nm feature was assigned to be from the A1 anion radical.⁵⁰

The kinetics of the CT process was sensitively tracked by measuring the rise of the excited state absorption (ESA) feature at 568 nm subsequent to 510 nm excitation. Figure 4b shows the sub-1 ps rise (could not be determined accurately due to field artifacts; see Figure S4, Supporting Information) of the kinetic signal at 568 nm which coincided with the simultaneous rise of the DMA cation radical at ~ 470 nm, thereby confirming the rise of the CT state within 1 ps. In aniline, however, the rise of the A1 anion radical ESA feature at 575 nm shown in the

inset of Figure 4b occurs within ~ 300 fs. The observed rise times in both aniline and DMA are in contrast to an instantaneous rise in non-redox-active solvent like toluene. Figure 4b (inset) shows the formation of the LE state in toluene which lives for almost ~ 540 ps. The appearance of the aniline radical cation at 420 nm (Figure S5, Supporting Information)³⁰ within a similar time scale confirms the ultrafast nature of the CT process. Therefore, it is evident that the ultrafast component obtained in the upconversion measurements truly represents the rate of the CT process.

In order to unequivocally demonstrate the conversion of the initially photoprepared LE state to the CT state, singular value decomposition (SVD) of the A1 in aniline data was carried out. Figure 4c shows the transient spectra of the two spectral components with lifetimes of ~ 370 fs and ~ 6 ps, respectively, used in the global fitting of the transient data. The ultrafast component matches the lifetime of the LE state in aniline, and therefore, the corresponding spectra can be assigned to a pure LE state. The distinct absorptive-emissive pattern of the LE spectra matches very well with the observed spectrum in non-redox solvents, e.g., methanol and toluene as enumerated in Figure S6 presented in the Supporting Information. The 6 ps spectral component matches very well with the A1 anion radical spectrum observed in the transient absorption kinetics of A1 in DMA. Thus, our transient pump–probe spectra show that the donor solvated A1 charge transfer rates are within the average time scale of ~ 300 – 700 fs in both aniline and DMA.

The CT state recombines to yield the neutral ground state in ~ 4 – 7 ps in aniline, while it lives longer in DMA as indicated by both the long fluorescence lifetime and excited state decay rates from transient absorption of ~ 7 – 10 ps.⁵¹ It should be noted that the CT state can be directly populated by excitations at the red edge of the LE band. In fact, an excitation wavelength dependence (at 560, 630, 650, 670, and 700 nm) quantifying the generated A1 radical anion population (using ΔA values at 570 nm) revealed that the CT optical transition is centered at 645 nm which was obtained using a Gaussian fit to the measured radical anion population (shown in Figure 4a). The presence of this weakly allowed CT band also provides an explanation of the broad wings for A1's absorption profile in DMA. The occurrence of a weakly allowed optical CT transition lower than the LE 0–0 transition (625 nm) as well

as the CT emission leads to our conjecture for the presence of only few well-defined donor–acceptor pairs which would control the charge transfer rates. Therefore, these spectroscopic signatures provide an experimental opportunity to visualize the Marcus non-adiabatic surface crossings both in terms of the coupling energetics and the reaction coordinate.

Evaluation of ET Parameters. The CT coupling strength required to obtain the observed rates was calculated using the semiclassical Marcus equation.⁵² Using the Rehm–Weller equation,⁵³ the driving force (ΔG°) was calculated on the basis of the donor and acceptor redox potentials along with the E_{0-0} of the LE. The reduction potential of A1 in methanol was experimentally ascertained via cyclic voltammetry (Figure S7, Supporting Information), while the previously reported oxidation potentials of DMA and aniline were used for the analysis.⁵⁴ The driving force for A1/DMA reaction was calculated to be weakly exergonic, $\Delta G^\circ \sim -0.69$ eV, while A1 in aniline had a slightly smaller value of ~ -0.56 eV (Table ST1, Supporting Information). Due to the lack of any observed temperature dependence to the CT rates in the range 277–323 K (Figure S8, Supporting Information), the electron transfer process occurs in the barrierless regime. The electronic coupling matrix element H_{CT} was calculated to be ~ 68 and ~ 96 cm^{-1} in DMA and aniline, respectively, indicating a primarily non-adiabatic crossing between the LE and CT states.²³ Due to the barrierless nature of the transfer, the Marcus crossing was identified to be close to the minima of the LE surface. Therefore, rather than having a stochastic process leading up to the Marcus crossing, the CT reaction coordinate becomes deterministic.

Resonance Raman Measurements. The 300–700 fs CT time scale compels us to actively probe the reaction coordinate through the window of the Franck–Condon dynamics, although the fastest transfer rates could be slightly slower than the experimentally obtained time scale.²⁴ The FC activity of the anthraquinone modes sets up the initial reaction trajectory and the search for the surface crossing. To examine the FC active modes, Raman spectra of A1 in DMA were collected across the LE resonance.⁵⁵ The resonance Raman intensities would allow for a mode-dependent information on the excited state displacements.⁵⁶ The RR spectra of A1 in DMA with excitation at 532 and 632.8 nm are shown in Figure 5. All the peaks were assigned on the basis of the DFT calculations⁵⁷ carried out at the B3LYP/6-311g(d,p) level in the gas phase and with implicit solvation.

The most prominent features seen in the RR spectrum at 257 (out-of-plane ring deformation), 447 (in-plane ring deformation near the hydroxy-keto group), 938, 1268 (C–O/C–C stretch), and 1400 cm^{-1} (C–N stretch) have Raman cross sections in the order of $\sim 10^{-10}$ $\text{\AA}^2/\text{molecule}$ (Table ST2, Supporting Information). There are other features at 674, 748, 1160, and 1604 cm^{-1} (C=O stretch) that have Raman cross sections an order of magnitude smaller than the largest cross section. It is noteworthy that the low frequency bands at 257 and 447 cm^{-1} along with the C=O stretch at 1604 cm^{-1} show remarkable enhancement in the intensity as the excitation wavelength changes from 532 to 647.1 nm (Figure S9, Supporting Information). The remarkable FC activity immediately implies an important role in driving the system toward the LE–CT crossing. The in-plane deformation mode at 447 cm^{-1} may couple strongly with the C=O stretch, which primarily arises from the stretching motions of the hydroxy-keto group. This unusual enhancement in the C=O stretch coupled to the

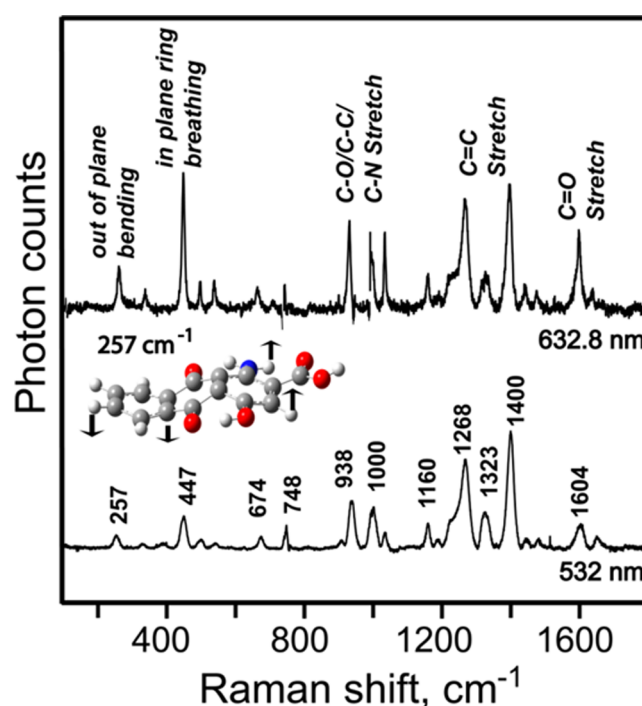


Figure 5. Normalized resonance Raman spectra of A1 in DMA at 532 and 632.8 nm excitation wavelengths. The normal modes were assigned on the basis of vibrational analysis of the DFT optimized A1 structure. The low-frequency modes at 257, 447, and 1604 cm^{-1} are enhanced anomalously at 632.8 nm.

in-plane deformation possibly hints at the stabilization of the incipient electron on the hydroxy-keto moiety in the A1 anion radical state. The 257 cm^{-1} mode described by the displacements in Figure 5 represents an out-of-plane ring deformation mode. Interestingly, the ~ 130 fs time period of the 257 cm^{-1} deformation mode matches closely to the time scale of the CT reaction. Therefore, the enhanced intensity of the 257 cm^{-1} indicates that the excited state displacements are large along this coordinate and the initial slope would direct the system toward the crossing.⁵⁸

Molecular Dynamics Simulations. Molecular dynamics simulations coupled with DFT calculations were used to gain a dynamic mechanistic insight by correlating the CT rates to the time scale of the deformation modes identified by resonance Raman. To establish a key role played by such deformation modes, a temporal correlation of low-frequency modes in the charge transfer reaction and the evolution of the CT coupling strengths (H_{CT}) of A1/DMA 1:1 D–A pairs in the primary solvation layer along a 9 ps MD trajectory was investigated. The coupling strengths between the LE and CT states (transitions shown in Figure 6) were calculated using a generalized Mulliken–Hush (GMH) approach^{40,59,60} based on TDDFT calculations⁴³ on the pairs within the first solvation layer as described previously in the computational methodology section. Previous work^{22,61} has reported that CT coupling strengths decay with the relative distances between the solute–solvent pairs, and hence, the solvent molecules in the primary layer, which extends up to 3.5 \AA , should be the key contributors in the overall electron transfer process. Figure 7a describes the edge-to-edge distance distribution function calculated via the nearest distances of the A1 and DMA molecules. The first solvation shell consists of ~ 20 DMA molecules, shown through a snapshot in Figure 7b, out of which some selective

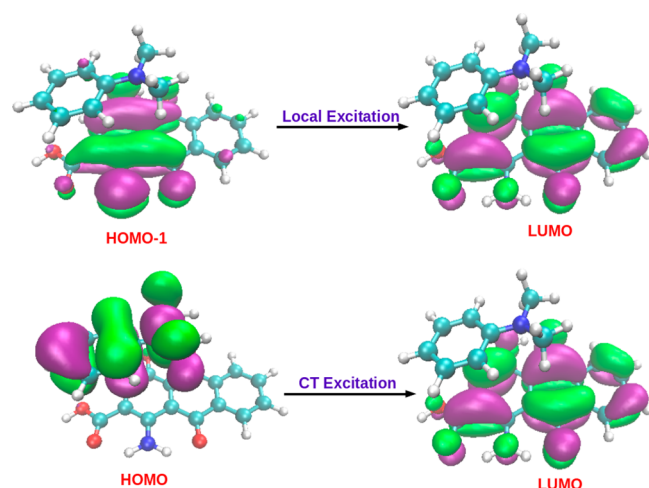


Figure 6. The frontier orbitals involved in the LE and CT excitations. The orbitals were plotted using VMD visualization software at an electronic isodensity of 0.02 au.

orientations should have favorable CT couplings. To compare the CT strengths in each of these specific configurations, we superimposed the CT coupling strengths on top of the histogram of edge-to-edge distances in Figure 7a. As evident from the large distribution of the CT coupling values ranging from 0.01 to 0.11 eV, only few such D–A pairs will likely have the strongest coupling values.

In order to choose the most important pair in terms of CT coupling strengths, the temporal variation in CT coupling in all the 20 A1/DMA pairs in the primary layer was calculated during the trajectory, as shown in Figure S10 (Supporting Information). We find that, for a cofacial A1/DMA pair in which the amine part of the solvent molecule faces the hydroxy-keto moiety (Figure S11, Supporting Information), the CT coupling strengths are much higher as compared to the rest of the molecules in the solvation shell during a considerable part of the dynamics.^{4,62} This was particularly evident in the 6 ps time slice where the CT coupling reaches its highest value. We evaluated the correlations between the molecular vibrations and dynamical modulation of the coupling strength for this pair, as shown in Figure S12 (Supporting Information). Interestingly our analysis on the CT couplings for all pairs in the primary

solvation shell validates our conjecture that only few D–A pairs are important for the charge transfer reaction, and the cofacial pair is intrinsically the most strongly coupled.

In the 6 ps time interval, we carried out short NVE simulations of length 1 ps to analyze the temporal variations of the coupling matrix elements and the nuclear motions of the dye on a finer time scale, as discussed in the computational methodology section. Figure 8a plots the temporal evolution of

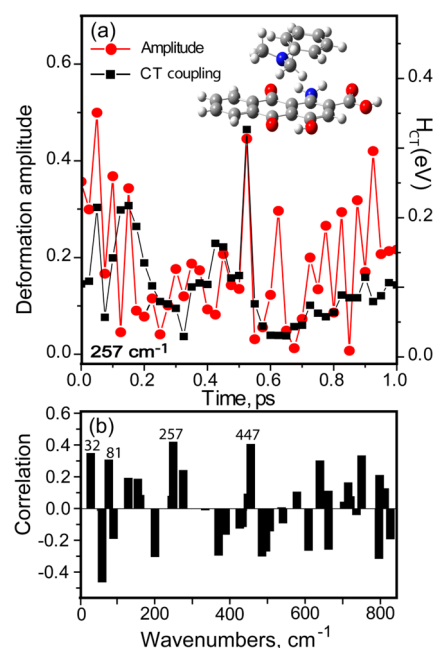


Figure 8. (a) Dynamic correlation of vibrational amplitude (red) of the 257 cm^{-1} mode with the CT coupling (black) in the cofacial 1:1 pair of A1/DMA obtained from the 25 fs snapshots in the MD trajectory described below. (b) Pearson correlation parameter plot for all low-frequency modes describing positive and anticorrelation to the CT couplings based on the cofacial pair.

the H_{CT} for this cofacial pair as well as the amplitude of the 257 cm^{-1} mode along the NVE trajectory starting from the 6 ps snapshot. The dynamic modulation of the coupling strength correlated well with the vibrational amplitude up to ~ 500 fs,

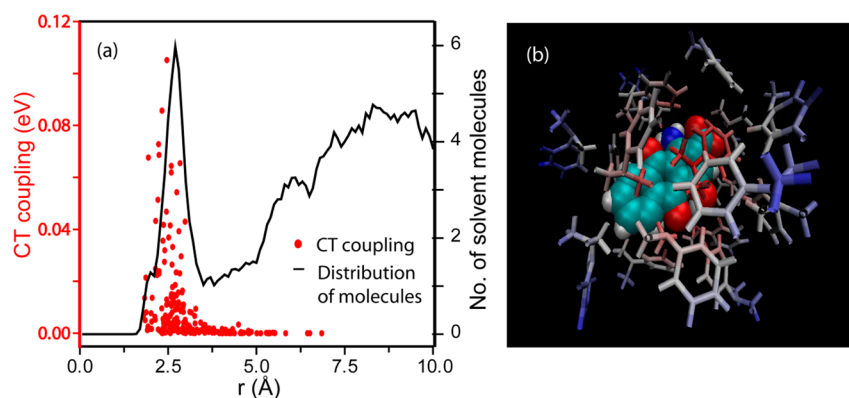


Figure 7. (a) A histogram of the number of solvent molecules plotted against the edge-to-edge distances between the DMA and A1. Superimposed is the corresponding CT couplings of all donor–acceptor pairs around A1. Edge-to-edge distance distribution for A1 in DMA marks a distinct peak at 2.5 Å which corresponds to the first solvation shell. We consider only those molecules within this shell as the putative electron donors. The dependence of ET coupling elements on the edge–edge distance for the solvation shell along the trajectory is shown in red dots. (b) A representative snapshot of the primary solvation shell from the MD trajectory.

which matches very well with the time scale of the CT reaction observed in the experiments. The strong temporal correlation of the CT coupling with vibrational amplitudes implies that the propensity for charge transfer is controlled via the ring skeletal motions leading to transfer rates faster than solvent reorientations. In fact, correlations with all the low-frequency modes below 1000 cm^{-1} shown in Figure 8b highlight that only selective modes have positive correlations. Interestingly, all the deformation modes at 32, 81, 257 (253 cm^{-1} in DFT), and 447 cm^{-1} (460 cm^{-1} in DFT) show high positive correlation. The 32 and 81 cm^{-1} modes correspond to global ring deformations (Figure S13, Supporting Information)⁶³ and have similar symmetries to the 257 cm^{-1} mode which we have illustrated in Figure 5. The magnitude of the correlations quantified by the Pearson coefficients matches very well with the resonance Raman intensities. Therefore, a fascinating concurrence in time scales emerges from our comparison of the resonance Raman and computational work, providing evidence that deformations facilitate the surface crossing. It also illustrates the power of resonance Raman methodology to unravel important modes which control excited state chemistry. It should be noted that such deformations at a local length scale have important functional consequences in describing properties like charge transport in nucleic acids.⁶⁴

Potential Energy Surface. The potential energy diagram in Figure 9 summarizes our principal findings and provides a

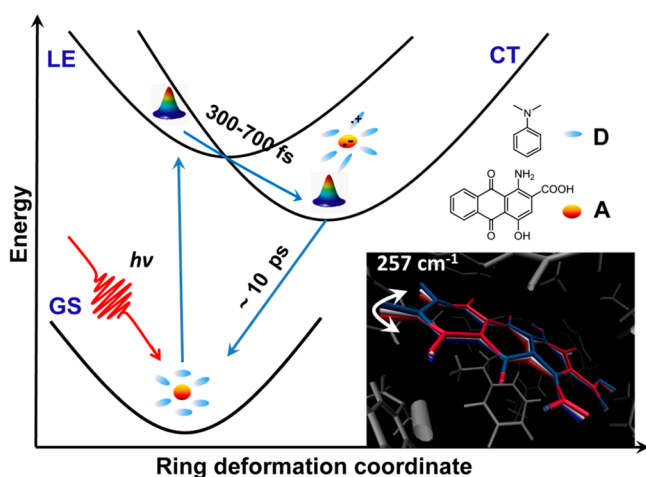


Figure 9. Potential energy scheme of the CT reaction. Upon light absorption to the LE state, the ring deformation coordinate becomes active and drives the system to the Marcus crossing. The solvation in the CT state later leads to the recombination back to the ground state. On the right bottom, the modulation of the 257 cm^{-1} mode in the 1:1 pair is shown in the context of the gating to achieve the CT state.

mechanistic insight into the CT process. Subsequent to the optical excitation of anthraquinone A1, the FC dynamics along the deformation modes lead the system to the LE–CT crossing by $\sim 300\text{--}700\text{ fs}$. The crossing is shown to be at the bottom of the potential well in the LE state, since the charge transfer process was found to be barrierless.⁶⁵ The recombination reaction yields the A1 ground state in DMA within $\sim 10\text{ ps}$ timescale which also operates in the barrierless regime. Although the reaction coordinate may involve multiple reactive motions that lead to the CT state via surface crossing, our work reveals that the 257 cm^{-1} mode is one of the key driving coordinates. The mode highlights the out-of-plane deformation motion of the anthraquinone ring (shown in the Figure 9 inset)

leading to dynamic proximity toward the DMA molecule in the cofacial D–A arrangement. It can easily be speculated that this motion would lead to greater orbital overlaps, and under favorable conditions set by initial solvent configurations, the ET reaction will take place efficiently. This significant understanding clearly enhances the need to use such motions deliberately for efficient charge transfer. In summary, our work provides a glimpse of the molecular nature of the CT reaction coordinate and implies the need for temporal tracking of all relevant reactive motions for uncovering new mechanistic insights.

CONCLUSIONS

We have demonstrated that deformation modes of the hydroxyanthraquinone skeleton are potent initiators for sampling reactive geometries to carry out effective electron transfer reactions. We anticipate that the sensitization of the weak CT transition in large preorganized structures can be aided by surrounding hydroxyanthraquinone with donors in correct cofacial arrangements. The stabilization of the negative charge preferentially on the hydroxy-keto moiety of A1 should motivate derivatization from the amine side. Following the design principles alluded to in this work, anthraquinones can potentially rival the more celebrated yet bulky fullerenes in complex light conversion assemblies.⁶⁶ Our work thereby underscores the importance of rationally positioning D–A pairs not just based on distance restraints but also based on the constraints set by the thermally accessible motions in non-covalent assemblies. We believe that this normal mode engineering approach will inspire new research to create functional materials more reliably over serendipitous self-assembly.

ASSOCIATED CONTENT

Supporting Information

Additional time-resolved data, electrochemistry, resonance Raman, and computational data are provided. This material is available free of charge via the Internet at <http://pubs.acs.org>.

AUTHOR INFORMATION

Corresponding Authors

*E-mail: dasgupta@tifr.res.in.

*E-mail: vardha@iiserb.ac.in.

Author Contributions

§A.J., D.C.: These authors contributed equally.

Notes

The authors declare no competing financial interest.

ACKNOWLEDGMENTS

The authors thank Dr. Anindya Datta and Anjali Dhir (IIT Bombay) for the fluorescence upconversion; and Dr. Shankar Ghosh and Ms. Smita Gohil (TIFR), and Dr. Chandrabhas Narayana and Soumik Siddhanta (JNCASR) for a few Raman measurements. Critical discussion with Dr. R. Venkatramani (TIFR) is acknowledged. D.C. thanks TIFR for Junior Research fellowship. J.D. thanks the Department of Atomic Energy for monetary support and the Tata Institute of Fundamental Research, Mumbai, for startup funds. V.S. and J.D. thank IISER Bhopal and TIFR for computational resources.

■ ABBREVIATIONS

DMA, *N,N*-dimethylaniline; NMA, *N*-methylaniline; LE, localized excitation; CT, charge transfer; MD, molecular dynamics; DFT, density functional theory

■ REFERENCES

- (1) Cook, T. R.; Zheng, Y. R.; Stang, P. J. Metal-Organic Frameworks and Self-Assembled Supramolecular Coordination Complexes: Comparing and Contrasting the Design, Synthesis, and Functionality of Metal-Organic Materials. *Chem. Rev.* **2013**, *113*, 734–777.
- (2) Ward, M. D.; Raithby, P. R. Functional Behaviour from Controlled Self-Assembly: Challenges and Prospects. *Chem. Soc. Rev.* **2013**, *42*, 1619–1636.
- (3) Bui, P. T.; Nishino, T.; Yamamoto, Y.; Shiigi, H. Quantitative Exploration of Electron Transfer in a Single Noncovalent Supramolecular Assembly. *J. Am. Chem. Soc.* **2013**, *135*, 5238–5241.
- (4) She, C. X.; Lee, S. J.; McGarrah, J. E.; Vura-Weis, J.; Wasielewski, M. R.; Chen, H. N.; Schatz, G. C.; Ratner, M. A.; Hupp, J. T. Photoinduced Electron Transfer from Rail to Rung within a Self-Assembled Oligomeric Porphyrin Ladder. *Chem. Commun.* **2009**, *46*, 547–549.
- (5) Wan, C. Z.; Fiebig, T.; Schiemann, O.; Barton, J. K.; Zewail, A. H. Femtosecond Direct Observation of Charge Transfer between Bases in DNA. *Proc. Natl. Acad. Sci. U.S.A.* **2000**, *97*, 14052–14055.
- (6) Reid, P. J.; Silva, C.; Barbara, P. F.; Karki, L.; Hupp, J. T. Electronic Coherence, Vibrational Coherence, and Solvent Degrees of Freedom in the Femtosecond Spectroscopy of Mixed-Valence Metal Dimers in H₂O and D₂O. *J. Phys. Chem.* **1995**, *99*, 2609–2616.
- (7) Barbara, P. F.; Meyer, T. J.; Ratner, M. A. Contemporary Issues in Electron Transfer Research. *J. Phys. Chem.* **1996**, *100*, 13148–13168.
- (8) D'Souza, F.; Chitta, R.; Sandanayaka, A. S. D.; Subbaiyan, N. K.; D'Souza, L.; Araki, Y.; Ito, O. Supramolecular Carbon Nanotube-Fullerene Donor-Acceptor Hybrids for Photoinduced Electron Transfer. *J. Am. Chem. Soc.* **2007**, *129*, 15865–15871.
- (9) D'Souza, F.; Ito, O. Supramolecular Donor-Acceptor Hybrids of Porphyrins/Phthalocyanines with Fullerenes/Carbon Nanotubes: Electron Transfer, Sensing, Switching, and Catalytic Applications. *Chem. Commun.* **2009**, 4913–4928.
- (10) Pauvert, M.; Laine, P.; Jonas, M.; Wiest, O. Toward an Artificial Oxidative DNA Photolyase. *J. Org. Chem.* **2004**, *69*, 543–548.
- (11) Kamioka, K.; Cormier, R. A.; Lutton, T. W.; Connolly, J. S. Charge-Transfer Emission in Meso-Linked Zinc Porphyrin Anthraquinone Molecules. *J. Am. Chem. Soc.* **1992**, *114*, 4414–4415.
- (12) Song, Z. P.; Zhan, H.; Zhou, Y. H. Anthraquinone Based Polymer as High Performance Cathode Material for Rechargeable Lithium Batteries. *Chem. Commun.* **2009**, 448–450.
- (13) Regan, J. J.; Risser, S. M.; Beratan, D. N.; Onuchic, J. N. Protein Electron-Transport - Single versus Multiple Pathways. *J. Phys. Chem.* **1993**, *97*, 13083–13088.
- (14) Beratan, D. N.; Betts, J. N.; Onuchic, J. N. Protein Electron-Transfer Rates Set by the Bridging Secondary and Tertiary Structure. *Science* **1991**, *252*, 1285–1288.
- (15) Skourtis, S. S.; Balabin, I. A.; Kawatsu, T.; Beratan, D. N. Protein Dynamics and Electron Transfer: Electronic Decoherence and Non-Condon Effects. *Proc. Natl. Acad. Sci. U.S.A.* **2005**, *102*, 3552–3557.
- (16) Li, G. Q.; Movaghar, B.; Ratner, M. A. Dynamic Electron Localization Initiated by Particle-Bath Coupling. *Phys. Rev. B* **2013**, *87*, 094302.
- (17) Kobayashi, T.; Takagi, Y.; Kandori, H.; Kemnitz, K.; Yoshihara, K. Femtosecond Intermolecular Electron-Transfer in Diffusionless, Weakly Polar Systems - Nile Blue in Aniline and *N,N*-dimethylaniline. *Chem. Phys. Lett.* **1991**, *180*, 416–422.
- (18) Yoshihara, K.; Tominaga, K.; Nagasawa, Y. Effects of the Solvent Dynamics and Vibrational Motions in Electron-Transfer. *Bull. Chem. Soc. Jpn.* **1995**, *68*, 696–712.
- (19) Seel, M.; Engleitner, S.; Zinth, W. , Wavepacket Motion and Ultrafast Electron Transfer in the System Oxazine 1 in *N,N*-dimethylaniline. *Chem. Phys. Lett.* **1997**, *275*, 363–369.
- (20) Wynne, K.; Reid, G. D.; Hochstrasser, R. M. Vibrational Coherence in Electron Transfer: The Tetracyanoethylene-Pyrene Complex. *J. Chem. Phys.* **1996**, *105*, 2287–2297.
- (21) Iwai, S.; Murata, S.; Katoh, R.; Tachiya, M.; Kikuchi, K.; Takahashi, Y. Ultrafast Charge Separation and Exciplex Formation Induced by Strong Interaction Between Electron Donor and Acceptor at Short Distances. *J. Chem. Phys.* **2000**, *112*, 7111–7117.
- (22) Castner, E. W.; Kennedy, D.; Cave, R. J. Solvent as Electron Donor: Donor/Acceptor Electronic Coupling is a Dynamical Variable. *J. Phys. Chem. A* **2000**, *104*, 2869–2885.
- (23) Scherer, P. O. J. Intramolecular Reorganization of the Electron Donor *N,N*-Dimethylaniline. *J. Phys. Chem. A* **2003**, *107*, 8327–8329.
- (24) Vauthey, E. Photoinduced Symmetry-Breaking Charge Separation. *Chemphyschem* **2012**, *13*, 2001–2011.
- (25) Morandeira, A.; Furstenberg, A.; Vauthey, E. Fluorescence Quenching in Electron-Donating Solvents. 2. Solvent Dependence and Product Dynamics. *J. Phys. Chem. A* **2004**, *108*, 8190–8200.
- (26) Morandeira, A.; Furstenberg, A.; Gumy, J. C.; Vauthey, E. Fluorescence quenching in electron-donating solvents. 1. Influence of the Solute-Solvent Interactions on the Dynamics. *J. Phys. Chem. A* **2003**, *107*, 5375–5383.
- (27) Murata, S.; Tachiya, M. Unified Interpretation of Exciplex Formation and Marcus Electron Transfer on the Basis of Two-Dimensional Free Energy Surfaces. *J. Phys. Chem. A* **2007**, *111*, 9240–9248.
- (28) Scherer, P. O. J.; Tachiya, M. Computer Simulation Studies of Electron Transfer Parameters for Cyanoanthracene/*N,N*-dimethylaniline Solutions. *J. Chem. Phys.* **2003**, *118*, 4149–4156.
- (29) Chatterjee, S.; Burai, T. N.; Karuso, P.; Datta, A. Ultrafast Dynamics of Epicoconone, a Second Generation Fluorescent Protein Stain. *J. Phys. Chem. A* **2011**, *115*, 10154–10158.
- (30) Kumar, G. V. P.; Narayana, C. Adapting a Fluorescence Microscope to Perform Surface Enhanced Raman Spectroscopy. *Curr. Sci.* **2007**, *93*, 778–781.
- (31) Frisch, M. J.; Trucks, G. W.; Schlegel, H. B.; Scuseria, G. E.; Robb, M. A.; Cheeseman, J. R.; Scalmani, G.; Barone, V.; Mennucci, B.; Petersson, G. A.; et al. *Gaussian 09*, revision A.1; Gaussian, Inc.: Wallingford, CT, 2009.
- (32) Rizzo, R. C.; Jorgensen, W. L. OPLS All-Atom Model for Amines: Resolution of the Amine Hydration Problem. *J. Am. Chem. Soc.* **1999**, *121*, 4827.
- (33) Jorgensen, W. L.; Maxwell, D. S.; Tirado-Rives, J. Development and Testing of the OPLS All-Atom Force Field on Conformational Energetics and Properties of Organic Liquids. *J. Am. Chem. Soc.* **1996**, *118*, 11225–11236.
- (34) Lindahl, E.; Hess, B.; van der Spoel, D. GROMACS 3.0: a Package for Molecular Simulation and Trajectory Analysis. *J. Mol. Model.* **2001**, *7*, 306–317.
- (35) Berendsen, H. J. C.; van der Spoel, D.; van Drunen, R. Gromacs: A Message-Passing Parallel Molecular Dynamics Implementation. *Comput. Phys. Commun.* **1995**, *91*, 43.
- (36) Berendsen, H. J. C.; Postma, J. P. M.; Van Gunsteren, W. F.; DiNola, A.; Haak, J. R. Molecular Dynamics With Coupling to an External Bath. *J. Chem. Phys.* **1984**, *81*, 3684.
- (37) Hoover, W. G. Canonical Dynamics: Equilibrium Phase-Space Distributions. *Phys. Rev. A* **1985**, *31*, 1695–1697.
- (38) Nose, S. A Molecular Dynamics Method for Simulations in the Canonical Ensemble. *Mol. Phys.* **1984**, *52*, 255–268.
- (39) Hess, B.; Bekker, H.; Berendsen, H. J. C.; Fraaije, J. G. E. M. LINCS: A Linear Constraint Solver for Molecular Simulations. *J. Comput. Chem.* **1997**, *18*, 1463–1472.
- (40) Cave, R. J.; Newton, M. D. Generalization of the Mulliken-Hush Treatment for the Calculation of Electron Transfer Matrix Elements. *Chem. Phys. Lett.* **1996**, *249*, 15–19.
- (41) Petersilka, M.; Grossman, U. J.; Gross, E. K. U. Excitation Energies from Time-Dependent Density-Functional Theory. *Phys. Rev. Lett.* **1996**, *76*, 1212–1215.

- (42) Salek, P.; Vahtras, O.; Guo, J.; Luo, Y.; Helgaker, T.; Agren, H. Calculations of Two-Photon Absorption Cross Sections by Means of Density-Functional Theory. *Chem. Phys. Lett.* **2003**, *374*, 446–452.
- (43) Runge, E.; Gross, E. K. U. Density-Functional Theory for Time-Dependent Systems. *Phys. Rev. Lett.* **1984**, *52*, 997.
- (44) Angeli, C.; Bak, K. L.; Bakken, V.; Christiansen, O.; Cimiraglia, R.; Coriani, S.; Dahle, P.; Dalskov, E. K.; Enevoldsen, T.; Fernandez, B.; et al. *Dalton 2011, DALTON, a Molecular Electronic Structure Program*; University of Oslo: Oslo, 2011.
- (45) Humphrey, W.; Dalke, A.; Schulten, K. VMD: Visual Molecular Dynamics. *J. Mol. Graphics* **1996**, *14*, 33–38.
- (46) Petrone, P.; Pande, V. S. Can Conformational Change be Described by Only a Few Normal Modes? *Biophys. J.* **2006**, *90*, 1583–1593.
- (47) Nagasawa, Y.; Yartsev, A. P.; Tominaga, K.; Bisht, P. B.; Johnson, A. E.; Yoshihara, K. Dynamical Aspects of Ultrafast Intermolecular Electron-Transfer Faster than Solvation Process - Substituent Effects and Energy-Gap Dependence. *J. Phys. Chem.* **1995**, *99*, 653–662.
- (48) Kandori, H.; Kemnitz, K.; Yoshihara, K. sub-picosecond Transient Absorption Study of Intermolecular Electron-Transfer Between Solute and Electron-Donating Solvents. *J. Phys. Chem.* **1992**, *96*, 8042–8048.
- (49) Wheeler, J.; Nelson, R. F. Electrochemical and Spectroscopic Studies of Cation Radicals 0.2. Anilinium-Type Radical Ion and Benidine Dication Visible Spectra. *J. Phys. Chem.* **1973**, *77*, 2490–2492.
- (50) Zhu, H. M.; Song, N. H.; Lian, T. Q. Wave Function Engineering for Ultrafast Charge Separation and Slow Charge Recombination in Type II Core/Shell Quantum Dots. *J. Am. Chem. Soc.* **2011**, *133*, 8762–8771.
- (51) Nagasawa, Y.; Yartsev, A. P.; Tominaga, K.; Johnson, A. E.; Yoshihara, K. Temperature-Dependence of Ultrafast Intermolecular Electron-Transfer Faster Than Solvation Process. *J. Chem. Phys.* **1994**, *101* (7), 5717–5726.
- (52) Marcus, R. A.; Sutin, N. Electron Transfers in Chemistry and Biology. *Biochim. Biophys. Acta* **1985**, *811*, 265–322.
- (53) Rehm, D.; Weller, A. Kinetics of Fluorescence Quenching by Electron and H-Atom Transfer. *Isr. J. Chem.* **1970**, *8*, 259–271.
- (54) Shirota, H.; Pal, H.; Tominaga, K.; Yoshihara, K. Substituent Effect and Deuterium Isotope Effect of Ultrafast Intermolecular Electron Transfer: Coumarin in Electron-Donating Solvent. *J. Phys. Chem. A* **1998**, *102*, 3089–3102.
- (55) Hupp, J. T.; Williams, R. D. Using Resonance Raman Spectroscopy to Examine Vibrational Barriers to Electron Transfer and Electronic Delocalization. *Acc. Chem. Res.* **2001**, *34*, 808–817.
- (56) Lee, S. Y.; Heller, E. J. Time-Dependent Theory of Raman Scattering. *J. Chem. Phys.* **1979**, *71*, 4777–4788.
- (57) Kohn, W.; Sham, L. J. Self-Consistent Equations Including Exchange and Correlation Effects. *Phys. Rev.* **1965**, *140*, 1133.
- (58) Myers, A. B.; Mathies, R. A. *Biological Applications of Raman Spectrometry*; John Wiley and Sons: New York, 1987.
- (59) Marcus, R. A. On Theory of Electron-Transfer Reaction. 6. Unified Treatment for Homogeneous and Electrode Reactions. *J. Chem. Phys.* **1965**, *43*, 679–701.
- (60) Hush, N. S. Intervalence-Transfer Absorption. *Prog. Inorg. Chem.* **1967**, *8*, 391.
- (61) Zheng, J.; Kang, Y. K.; Therein, M. J.; Beratan, D. N. Generalized Mulliken-Hush Analysis of Electronic Coupling Interactions in Compressed π -Stacked Porphyrin-Bridge-Quinone Systems. *J. Am. Chem. Soc.* **2005**, *127*, 11303–11310.
- (62) Northrop, B. H.; Zheng, Y. R.; Chi, K. W.; Stang, P. J. Self-Organization in Coordination-Driven Self-Assembly. *Acc. Chem. Res.* **2009**, *42*, 1554–1563.
- (63) Ge, M.; Zhao, H. W.; Wang, W. F.; Yu, X. H.; Li, W. X. Terahertz Time-Domain Spectroscopic Investigation on Quinones. *Sci. China, Ser. B: Chem.* **2008**, *51*, 354–358.
- (64) Hatcher, E.; Balaeff, A.; Keinan, S.; Venkatramani, R.; Beratan, D. N. PNA Versus DNA: Effects of Structural Fluctuations on Electronic Structure and Hole-Transport Mechanisms. *J. Am. Chem. Soc.* **2008**, *130*, 11752–11761.
- (65) Horke, D. A.; Li, Q.; Blancafort, L.; Verlet, J. R. R. Ultrafast Above-Threshold Dynamics of the Radical Anion of a Prototypical Quinone Electron-Acceptor. *Nat. Chem.* **2013**, *5*, 711–717.
- (66) Koeppe, R.; Sariciftci, N. S. Photoinduced Charge and Energy Transfer Involving Fullerene Derivatives. *Photochem. Photobiol. Sci.* **2006**, *5*, 1122–1131.